Applied Thermal Engineering 246 (2024) 122887

Contents lists available at ScienceDirect

Applied Thermal Engineering

journal homepage: www.elsevier.com/locate/apthermeng

Research Paper

Enhancement of a radiant floor with a checkerboard pattern of two PCMs for heating and cooling: Results of a real-scale monitoring campaign

Silvia Cesari *, Eleonora Baccega, Giuseppe Emmi, Michele Bottarelli

Department of Architecture, University of Ferrara, Via Quartieri 8, Ferrara 44121, Italy

ARTICLE INFO

Keywords:
Phase change materials (PCMs)
Radiant floor
Heating
Cooling
Peak load shifting
Experimental investigation

ABSTRACT

When integrated in radiant floor, phase change materials (PCMs) enable the system to store and release thermal energy in winter and efficiently mitigate heat gains in summer. Although a large number of studies examined the thermal performance of radiant floors with PCMs, most of the works conducted a numerical analysis. Only a few studies experimentally investigated PCM integrated radiant floors, and they were limited to laboratory set-ups. In addition, nearly all the works focused exclusively on space heating. A radiant floor enhanced with PCMs was experimentally investigated at large-scale within the H2020 European project IDEAS. The system was composed of two types of PCMs, one for heating and one for cooling, installed in a building demonstrator equipped with an existing air handling unit (AHU). Data showed that in summer thermal loads were absorbed by PCM during the day. Heat was then released in the night to maintain indoor temperature close to the setpoint. In winter, the radiant floor integrated with the AHU allowed to achieve 13 % energy savings compared to the sole AHU. PCM thermal storage allowed to maintain the setpoint temperature of 20 °C from 9 h up to almost 30 h after the switching off of the systems.

1. Introduction

Since the start of the energy crisis in September 2021, the European Commission has adopted urgent measures to tackle the issue. Firstly, a 15 % reduction in gas demand from all consumers was strongly encouraged, and obligation to reduce electricity consumption by at least 5 % during peak price hours was imposed [1]. Furthermore, at the end of March 2023 the EU Council and the Parliament reached a provisional agreement aimed at increasing the target of renewable energy from the existing 32 % to at least 42.5 % within 2030, with a specific benchmark of 49 % for building energy consumption [2]. For this reason, there is a growing interest in low-temperature heating and high-temperature cooling systems. Furthermore, in order to improve the exploitation of renewable energy sources, extensive studies have been focusing on technologies able to achieve peak load shifting and shaving, which enable to overcome the mismatch between supply and demand, thus facing the issue of renewable intermittency.

Compared to conventional heating systems using supply water temperatures of about 60–70 °C, water temperature reduced up to 35 °C or lower is adopted in radiant floor (RF) ones [3,4]. Similarly, RF cooling systems operate at significantly higher temperatures than 8 °C, which are commonly used in conventional systems [5]. Water temperature equal to or higher than 16 °C is usually employed for radiant cooling. The small temperature difference from indoor comfort temperature does not only allow RF systems to achieve considerable energy and costs savings both on heating and cooling [6,7], but also to foster the exploitation of renewables [8,9].

Within this background, the integration of PCMs in RF systems allows to further lower energy consumption, and especially foster the exploitation of renewable energy sources, as well as cut CO2 emissions [10,11]. With a theoretical volumetric storage density of up to 15 times higher than traditional storage materials [12], phase change materials (PCMs) are able to accumulate and discharge an important amount of thermal energy as latent heat while undergoing a change in phase [13]. During the day in winter, the PCM can store the available renewable heating loads, and subsequently emit them at comfort temperature in the night. Moreover, the PCM is able to ensure sufficient thermal resilience to absorb thermal loads. Then, these loads can be released by the available renewable cooling sources [14]. Therefore, PCMs integrated in RF systems can shave peak loads and shift energy consumption from high-demand to low-demand hours, when pricing is lower [15,16].

Considered their high energy saving potential, the energy performance of PCM enhanced RF systems has been examined by a very large

* Corresponding author.
E-mail address: silvia.cesari@unife.it (S. Cesari).

https://doi.org/10.1016/j.applthermaleng.2024.122887
Received 15 August 2023; Received in revised form 29 February 2024; Accepted 5 March 2024
Available online 6 March 2024

Nomenclature

Acronyms

AHU	Air handling unit
AHX	Air section
FEP	Fluorinated ethylene propylene
GHX	Geothermal field
HF	Heat flux
HDPE	High-density polyethylene
HP	Heat pump
PCM	Phase change material
PV/T	Photovoltaic/thermal collector
PVT_C	Solar section
RF	Radiant floor
RH	Relative humidity
S17	PCM with melting temperature of 17 °C
S27	PCM with melting temperature of 27 °C
XPS	Extruded polystyrene

Symbols

c_p	Specific heat [kJ/(kg·K)]
E	Energy [kWh]
m	Mass per unit surface area [kg/m^2]
$\dot{q}$	Heat flux [kW/m^2]
T	Temperature [K]
ΔH_{SL}	Latent heat [kJ/kg]
ΔT	Temperature difference [K]
Δx	Thickness [m]

Greek Symbols

ρ	Density [kg/m^3]
λ	Thermal conductivity [W/(m·K)]

Subscripts

el	electrical
f	floor
in	inlet
m	melting point
r	room
t	thermal
t_1	initial time
t_2	final time
tot	total

number of studies. Nevertheless, analysis of the literature has uncovered a shortage of experimental works investigating the application of PCMs in RF heating and cooling systems. Indeed, the majority of the studies only conducted a numerical analysis and focused exclusively on heating systems. The few experimental works used small-scale laboratory set-ups or test rooms at most. Therefore, systems providing space cooling result to be still unexplored.

Against this background, the present work aims at filling the current knowledge gap. Indeed, the study presents the first full-scale installation of a PCM integrated RF. The system was realised in a 100 m^2 snack-bar at the service of a vast academic complex, thus daily frequented by students, professors, technical staff and common people. Therefore, the novelty of the work is not only represented by the full-scale experimental investigation, but also by the fact that the system is actually, currently and continuously used in a public building. Furthermore, the RF analysed does not only provide space heating, but also cooling. For this reason, the study is characterised by strong significance compared to the current literature. In addition, innovation is also included in the respective position of the two types of PCM (the one destined for the heating period and the other one for the cooling season), which has never been adopted before. In fact, the works that analysed systems providing space heating and cooling always supposed the two PCM layers to be one above the other. Differently, in the present study the two PCMs were installed alternatively, in a checkerboard pattern. Finally, the system here presented was designed to be installed in an existing floor structure, thus, to be compatible with existing structural constraints often characterised by a particularly limited thickness. Also this issue has been rarely analysed in literature. Therefore, the work could be exploited to lay the basis for the design of far more optimised systems and to develop a design framework for a more extensive application of PCM enhanced radiant floor systems, especially considered the energy savings achievable through the adoption of these low-temperature heating and high-temperature cooling systems, as well as the potential exploitation of renewable energy sources.

In the following lines a review of the literature about PCM integrated RF systems is reported and is summarised in Table 1. A distinction between the studies that carried out exclusively a numerical analysis (identified as *N* in Table 1), those based on experimental tests (*E* in Table 1) and those involving both a numerical and experimental investigation (*N&E* in Table 1) is conducted, and dimensions of the set-up or test room, when adopted, are provided. Furthermore, the difference between the works focused on heating systems (*H* in Table 1) and those which considered systems providing both heating and cooling (*H&C* in Table 1) is highlighted. In addition, the position of PCM in relation to the piping network is specified, and especially the relative position when a PCM for heating and one for cooling were considered, in order to properly highlight the novelty of the present study. Finally, the main findings in terms of energy savings, floor surface temperature (T_f), room temperature (T_r), temperature (T) fluctuations, etc. are reported. In order to allow a proper interpretation of the results, the main operating conditions are also specified, like PCM melting point (T_m) and inlet water temperature (T_{in}).

Taking into account numerical studies about RF heating systems integrated with PCMs, a few works focused on examining the impact of PCM position in relation to piping on the thermal performance of the system. Plytaria et al. [17] compared a PCM with a melting point of 29 °C installed above or under pipes. Supply water at 40 °C was considered. The under-piping structure resulted to be the optimal scenario. PCM was assumed to be positioned below pipes also by Baek and Kim, who numerically examined macroencapsulated PCM having a melting point of 42 °C. The optimal supply water temperature was identified in the range 40–41 °C [18], and up to 15.3 % energy savings were evaluated with a 20–50 mm PCM layer [19]. Differently, Gonzalez and Prieto [20] investigated the performance of paraffin PCM bands embedded in concrete and positioned in contact and not in contact with pipes. The former led to melting rates increased up to 4.6 times, whilst a solidification process up to 1.8 times faster was achieved with the latter. Babaharra et al. [21] examined the impact of pipe spacing (from 11 to 18 cm) and PCM type (hydrated salt with 27 °C melting point and n-octadecane with 30 °C) assuming supply water at 35 °C. The analysis highlighted an improved heat transfer with microcapsules hydrated salt positioned above pipes. Furthermore, a higher pipe spacing corresponded to a longer melting process, thus to a better thermal comfort. Again, significantly smaller temperature fluctuations were found by Zhao et al. [22] for a PCM-RF compared to a common concrete system, equal to about 1 °C for the former and 5 °C for the latter, respectively. PCM was considered filling the space between pipes and over them. A PCM-RF coupled with a heat pump was simulated in Mazo et al. [23]. Granulated PCM with a melting point of 27 °C was integrated in the concrete slab encasing water pipes. Supply water at 33 °C was

Table 1
List of the reviewed papers about PCM integrated RFs, distinguished between numerical (N) and experimental (E) analysis and between heating (H) and cooling (C) systems.

Ref.	Heat./ Cool.	Method	Experimental set-up	PCM position	Key results
[17]	H	N	–	Above vs under piping	PCM under piping was the optimal scenario. Auxiliary loads reduced by 65 %.
[18]	H	N	–	Under piping	Optimal T_{in} = 40–41 °C to achieve T_r = 21.6–22.6 °C.
[19]	H	N	–	Under piping	Energy saving from 7.3 to 15.3 % with 20–50 mm PCM.
[20]	H	N	–	Above and between piping	PCM in contact with the piping: melting rates increased up to 4.6 times. PCM not in contact with pipes: solidification up to 1.8 times faster.
[21]	H	N	–	Above	15 % microcapsules hydrated salt above pipes with 18 cm pipe spacing was the optimal scenario.
[22]	H	N	–	Above and between piping	Smaller T fluctuations were found for the PCM-RF (1 °C) compared to common concrete RFs (5 °C).
[23]	H	N	–	Encasing piping	Total shift of the electric energy consumption, with a 18 % cost saving potential.
[24]	H	E	3.6 m^2 x 2.4 *m*	Under piping	T_{floor} = 32 °C when the system was on; $T_{floor} \cong$ 30 °C even after 8 h since the turning-off, with $T_r \cong$ 29 °C.
[26]	H	E	5.5 m^2 x 2.0 *m*	Above and between piping	PCM provided a higher and more stable heat supply than sand for longer time, as well as a more even T_{floor}.
[27]	H	E	38.5 m^2 x 2.4 *m*	Above piping	Only 42 % of the supplied heat was effectively employed for the storage.
[28]	H	N&E	0.3 x 0.4 x 0.1 m^3	Under piping	Optimal T_m = 38–45 °C to achieve T_r = 22 °C and T_{floor} = 28–30 °C.
[29]	H	N&E	0.5 x 0.5 x 0.095 m^3	Above piping	Much lower T_f fluctuation compared to standard slab. Thermal comfort was ensured despite 8 h-operation.
[30]	H	N&E	0.6 x 0.6 x 0.22 m^3	Above vs under piping	Mortar with high thermal conductivity and PCM under piping allowed to optimise T_{in} and achieve a 75 % higher heat flux.
[31]	H	N&E	0.6 x 0.6 m^2	Encasing piping	The PCM-graphene mortar showed lower T_{floor} fluctuations compared with a standard one, and a higher T_r when the system was off.
[32]	H	N&E	25.6 m^2 x 2.7 *m*	Wrapping piping	PCM at the end of the loop not all melted. Achievable small T_r fluctuations through intermittent heating.
[33]	H	N&E	25.6 m^2 x 2.7 *m*	Wrapping piping	Optimal pipe spacing = 28 cm and PCM thickness = 2 cm.
[34]	H&C	N	–	Above piping, cold storage layer above and heat one below	Energy released during heating and cooling increased by 41.1 % and 37.9 % compared to a standard RF.
[35]	H&C	N	–	Encasing piping, cold storage layer above and heat one below	Theoretical basis for the design of intermittent cooling and heating systems was provided.
[36]	H&C	N	–	Encasing piping, cold storage layer above and heat one below	T_{floor} = 18–24 °C with T_r = 19 °C (H) and T_{floor} = 19–24 °C with T_r = 26 °C (C).
[37]	H&C	E	0.4 x 0.4 x 0.6 m^3	Encasing piping, heat storage layer above vs below the cold one	Optimal configuration: upper heat storage layer; achievable heating and cooling energy savings of 58.6 % and 64 %.
[38]	H&C	E	1 m^2	Encasing piping, heat storage layer above vs below the cold one	Upper heat storage layer resulted in a much higher T_r and T_{floor} at the end of the thermal storage, but also in a higher T fluctuation during the heat release.
[14]	H&C	N&E	0.5 x 0.5 x 0.1 m^3	Encasing piping	In summer: cooling water reduced by 25 %. In winter: no impact on the system performance.
[39]	H&C	N&E	10.8 m^2 x 2.7 *m*	Above piping, different distributions of cold and heat storage layers	Weather forecast-based control brought to 4 % and 8 % heating and cooling energy savings.

considered. Results showed an achievable total shift of the electric energy consumption and a cost saving potential of nearly 18 %.

Differently from numerical studies, only a small number of experimental works was carried out about PCM-RF heating systems, and they were mostly limited to small-scale laboratory set-ups or test rooms at most. The installation of a PCM-RF heating system compatible with an existing floor structure was investigated for the first time by Park and Kim [24], which considered a 3.6 m^2 test room. PCM with a melting temperature of 44 °C was positioned under piping operating with supply water at 55 °C. Floor surface temperature reached 32 °C when the system was on, therefore decisively higher than the limit value of 29 °C defined by regulation [25]. A 5.5 m^2 test room was used by Zhou and He [26] to compare the thermal performance of a RF integrated with sand or with PCM positioned above and between pipes. Results demonstrated that PCM provided a higher and more stable heat supply for longer time, as well as a more even floor surface temperature. Differently from the studies mentioned above, Yamaguchi et al. [27] analysed a larger test room (38 m^2), but the space was not provided with windows, therefore it was not so realistic.

A larger number of studies conducted both a numerical and an experimental analysis about PCM-RF heating systems. Suitable melting temperatures for an organic PCM installed under piping were identified in 35, 37, 41 and 44 °C by Baek and Park [28]. Then numerical results were experimentally evaluated using a 0.3 x 0.4 x 0.1 m^3 set-up, which demonstrated that 41 °C was the best melting point. The thermal performance of a RF integrated with hydrated salt PCM was tested by Farid and Kong [29] using a 0.5 x 0.5 x 0.095 m^3 set-up. The macro-encapsulated PCM having a melting temperature of 28 °C was included in the concrete slab above piping. Results showed a decisively lower floor surface temperature fluctuation than a standard slab, and an acceptable surface temperature during the whole day despite the only 8 h-operation. The system was then numerically analysed for optimisation. A similarly small set-up (0.6 x 0.6 x 0.22 m^3) was used by Larwa et al. [30] to calibrate a numerical model and analyse the effect of PCM above or under heating pipes. Mortar with high thermal conductivity (i.e. wet sand) and PCM under piping allowed to optimise supply water temperature and achieve a heat flux 75 % higher than the above-piping configuration. Again, a 0.6 x 0.6 m^2 set-up was used by Baccega et al. [31] to test a mortar encasing piping and enhanced with paraffin PCM and graphene. PCM melting point was 28 °C and supply water temperature was between 35 and 40 °C. The system was then numerically investigated. Significantly lower floor temperature fluctuations were achieved compared with a standard mortar, and a 2.5 °C higher room temperature was ensured for 2 h more when the system was off. Differently, a larger test-room of 25 m^2 was adopted by Lu et al. [32] to test a double pipe PCM-RF system. Supply water temperature of 50 °C and paraffin PCM with a melting point of 36 °C were used. Findings showed that the PCM at the end of the loop did not melt completely. Then, the impact of pipe spacing, solidification temperature and PCM thickness was numerically analysed to optimise the system in the following work [33].

Whilst several studies investigated PCM-RF heating systems, a small

number of works focused on systems providing both space heating and cooling. Among these, even a smaller number conducted an experimental analysis. All the numerical studies reported below considered the cold PCM layer placed above the PCM for heating. A melting point of 28 °C for space heating and 17 °C for cooling were numerically investigated by Xu et al. [34], while 38 °C and 18 °C were selected by Jin and Zhang [35]. The latter found that the energy released by the PCM-RF was 41.1 % and 37.9 % higher during heating and cooling than a standard system. A RF using PCMs with a melting temperature of 30 °C for heating and 19 °C for cooling was numerically investigated by Ren et al. [36]. Results showed that floor surface temperature could be ensured in the range 18–24 °C with an indoor temperature of 19 °C during the heating period, while a floor surface temperature between 19 and 24 °C could be maintained in summer, with a room temperature of 26 °C.

As already mentioned before, only a few works experimentally examined RF systems providing heating and cooling, and all of them focused on the impact of the respective position of the two PCM layers. Nevertheless, differently from the findings of the numerical studies reported before [34–36], experimental results demonstrated that the heat storage layer placed above the cold storage one was the optimal layout. Heating and cooling energy savings of 58.6 % and 64 %, compared to a standard RF, were evaluated by Sun et al. [37] using a small set-up (0.4 x 0.4 x 0.6 m^3) with piping encased in PCM. A melting point of 31 °C was selected for the winter and 20 °C for the summer, operating with supply water at 42 °C and 10 °C, respectively. Again, a small test box with a floor surface of nearly 1 m^2 was used by Xia and Zhang [38] to compare the respective position of the two PCM layers encasing pipes. A melting point of 34 °C was assumed for the winter and 19 °C for the summer. Results highlighted an indoor air temperature about 6 °C higher during the heat release process with the heat storage layer above.

A very limited number of studies carried out both a numerical and experimental analysis on RF heating and cooling systems. Ansuini et al. [14] used small laboratory set-ups of 0.5 x 0.5 x 0.1 m^3 to investigate organic PCM granules having a melting point of 27 °C and encasing piping. Supply water at 35 °C for heating and 23 °C for cooling was adopted. Optimised numerical models were then developed. Results showed a 25 % reduction in cooling water, but no impact was observed on the heating behaviour. However, a PCM-RF heating and cooling system was experimentally investigated in a more realistic small experimental building only by Cesari et al. [39]. The system, which represents the small-scale prototype of the system described in the present study, was installed in a 10 m^2 test-room and then numerically investigated to define a weather forecast-based control strategy. A comprehensive description of the work is reported in section 2.1.

Against this background, a PCM enhanced RF providing space heating and cooling was experimentally examined for the first time at full-scale. The system was installed and analysed by the University of Ferrara (UNIFE) in the 100 m^2 snack-bar of the Department of Biomedical and Specialties Surgical Sciences of UNIFE within the H2020 European project IDEAS [40], and it is being monitored since end-June 2022. Results of the monitoring data for the heating and cooling period are here reported.

2. Methodology

2.1. Large-scale prototype

The objective of IDEAS project is the development of a novel low-cost building integrated renewable energy systems (RES) which will cost-effectively exceed current RES efficiencies, generating electricity, heat, and cooling and that will be optimised in different climatic conditions. Within this frame, the work package n.5 was focused on the large-scale installation of the IDEAS system in two demo sites, one located in Ferrara (Italy) and the other one in Mayo (Ireland). The piping and instrumentation diagram of the Italian large-scale prototype of the IDEAS system is reported in Fig. 1. The system implements a 25 kW multi-source water-to-water heat pump (HP), which operates by means of two primary loops between two tanks, a 800 l buffer tank on the source-side (identified as BF1) and two tanks of 500 l each one on the user-side (identified as BF2.1 and BF2.2), which are connected in series.

On the source side, the buffer tank BF1 is connected to the main loop of the system, which is fed by the pump P1. Buffer tanks were included in the system in order to avoid hydraulic issues and to ensure a proper management of the energy sources and terminal units, which requires a specific control of the fluid flowrate in the secondary loop. These requirements brought to the installation of two additional pumps on the secondary loop (P2 and P3).

In the primary loop the system operates between three thermal

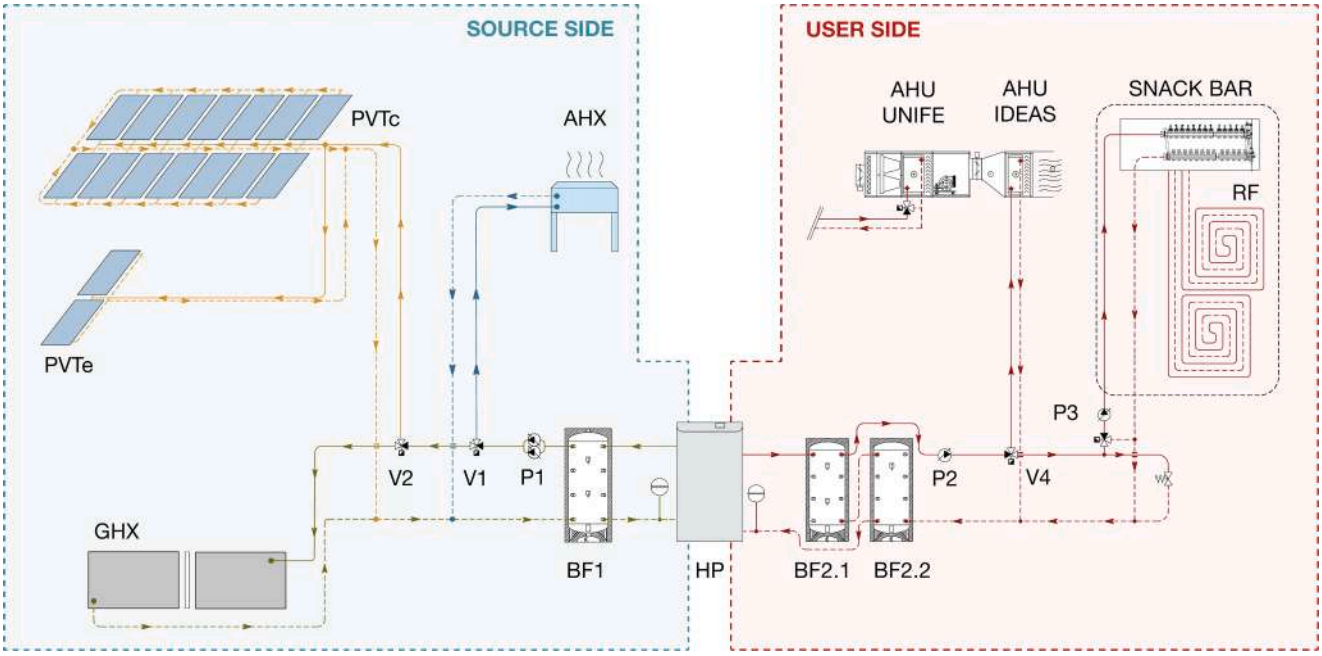

Fig. 1. Piping and instrumentation diagram of the large-scale prototype of the IDEAS system.

Fig. 2. Building demonstrator in Ferrara, Italy.

sources (ground, sun and air) to optimise the temperature on the source-side for the air-conditioning of the building demonstrator. The three thermal sections can operate separately or simultaneously and include the geothermal field (identified as GHX), the solar section (PVTc) and the air section (AHX), which employs a dry-cooler unit (20 kW_t, 0.5 kW_{el}) for the disposal of the heat coming from the PVTc or to regenerate the ground. The GHX loop is composed of 46 shallow ground heat exchangers (UNIFE patent EP2418439A2) [41], organised in 7 lines and installed in 2.5 m deep trenches, resulting in 92 m of GHXs, equal to more than 10 kW continuous peak power. More details about this type of shallow ground heat exchangers and their applications can be found in Refs. [42,43]. The solar section consists in 14 commercial photovoltaic/thermal panels (PV/T) (400 W of peak each one) horizontally installed on the roof of the demo building. This section also includes the connection of two experimental compound parabolic photovoltaic thermal collectors (identified as PVTe) vertically installed, which are not considered in the present analysis due to their negligible thermal and electric contribution.

On the user-side, a RF integrated with PCMs was installed in the area of the snack bar destined for clients. The space was equipped with an existing air handling unit (AHU) to ensure ventilation rates and manage latent loads. The existing AHU was modified by integrating a new section connected to the IDEAS system. In this way, the new experimental system allows to use, individually or simultaneously, the existing AHU as modified with the new IDEAS section and the novel RF system. This design approach ensures HVAC operation regardless of the state of the experimental plant, especially in the first start-up period, which required a lot of time spent for the testing and updating the management and logging data systems.

The snack-bar is a 1-storey volume adjacent to the academic building on two sides, and facing south-east with one façade, south-west with two façades and north-west with another façade (Fig. 2 and Fig. 3). Entrance is allowed both from the adjacent department and directly from outside. External walls are floor-to-ceiling windows with a painted iron frame and a single pane. Internal walls include a masonry wall and a glass partition with a painted iron frame. The flat roof is composed of a 30 cm suspended ceiling for piping and a 30 cm slab (beams and hollow clay blocks) covered with a bituminous waterproofing membrane coated with mineral granules. Values for surface, thickness and thermal transmittance of the components of the building envelope are reported in Table 2. Therefore, due to the largely glazed and hardly insulated building envelope, the snack-bar is characterised by a high energy demand both for space heating and cooling. The relevant energy demand is also due to the continuous flow of people coming in and out both from the adjacent department and directly from outside.

The space is characterised by a conditioned volume of nearly 442 m^3 and a conditioned floor surface of almost 134 m^2, which can be distinguished into two areas: one zone occupied by the counter and the other one destined for the clients (110 m^2), where the PCM integrated RF was installed.

The PCM enhanced RF system had been previously extensively investigated, both numerically and experimentally, firstly at lab-scale and then in a small mock-up building. The thermal behaviour of a RF heating system integrated with PCMs positioned above or below pipes was investigated by Larwa et al. [30] through numerical analysis and experimental tests carried out on lab-scale set-ups. Hydrated salts encapsulated in high-density polyethylene (HDPE) containers named ThinICE [44] – provided by PCM Products Ltd [45], partner of IDEAS project – were used. Results demonstrated that the under-piping scenario achieved an increase of 75 % in heat flux and a floor surface temperature 1.5 °C higher compared to the system with PCM positioned above piping. The under-piping configuration was further numerically and experimentally analysed within the work package n.3 (WP3 leader: UNIFE), through the installation in a small experimental building (10 m^2) located at the TekneHub laboratory of UNIFE, with the first findings reported in [39]. The RF system provided both space heating and cooling and it was enhanced with ThinICE having a melting point of 27 °C for the winter and 21 °C for the summer period.

The final and optimised prototype of the PCM enhanced RF system installed in the large-scale demo-building was composed of about 420 ThinICE with a melting temperature of 27 °C for the winter (called S27) and likewise with a melting point of 17 °C for summer (named S17) [46], which were positioned alternatively. A plan of the snack-bar with the distribution of PCMs containers and sensors is illustrated in Fig. 3, while the structure of the PCM-RF with the sensors position is reported in Fig. 4. The installation required the demolition of the existing floor (20–22 cm) and the realisation of a new structure having the same overall thickness. Thus, the coupling technology employed represents a

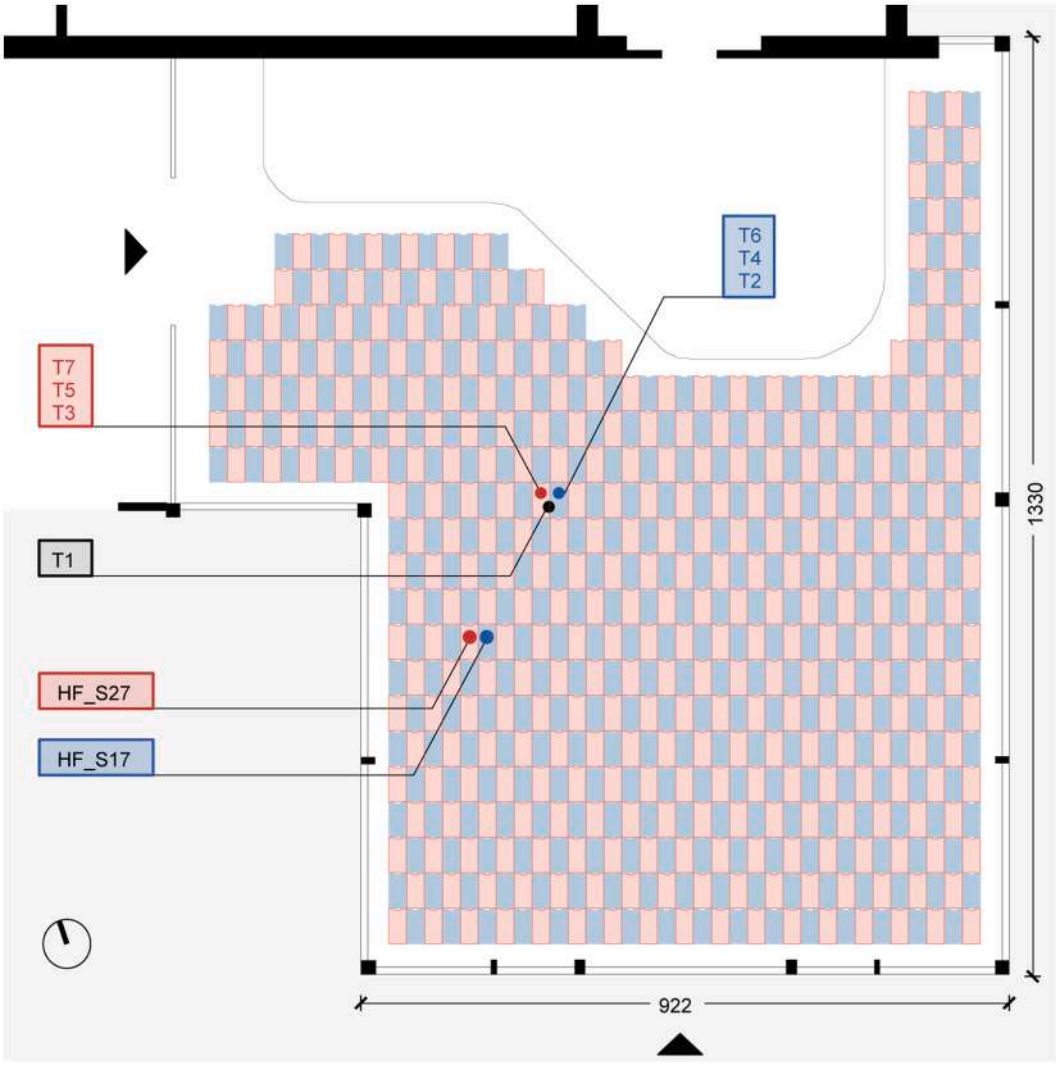

Fig. 3. Plan of the demo-building with the distribution of PCM containers and sensors.

Table 2
Demo-building physics.

Component	Surface m^2	Thickness m	Thermal transmittance $W/(m^2 \cdot K)$
Glazed external wall	128	0.005	5.00
Floor	134	0.215	0.64
Roof	134	0.400	1.40

real example of renovation providing high thermal storage through the installation of PCMs in a particularly limited thickness due to existing structural constraints.

The system is composed of a commercial vinyl flooring (1) installed over a 50 mm dry-set mortar (2). The mortar is characterised by high thermal conductivity and is improved with macro-synthetic fibre for screed reinforcement. Then, Ø16 x 2 mm piping (3) was installed above ThinICE (4) with a pitch of 80 mm (Fig. 5). ThinICE were positioned alternating S27 and S17 (Fig. 6) above a vapor barrier (5) covering a 40 mm high-density insulation panel (XPS300) (6). The panel was protected by a dump-proof membrane (7) placed between the insulation layer and a 80 mm concrete slab (8). The slab was improved with a waterproof additive and included a metal mesh. Floor structure materials and their thermophysical properties are reported in Table 3.

2.2. Monitoring system

The monitoring system included heat flux meters (produced by Hukseflux) [47] and T-type thermocouples (manufactured by Delta Strumenti) [48], positioned as illustrated in Fig. 3 and in Fig. 4. Heat flux meters were made of a thermopile protected by a ceramic plastic composite body, suitable and reliable for long term installations with IP67 protection. T-type thermocouples (copper and constantan) with fluorinated ethylene propylene (FEP) sheath were selected as the application required a small temperature detector.

Indoor air temperature was monitored by a digital temperature (T) and humidity (RH) sensor (manufactured by S + S Regeltechnik) [49] placed in the snack-bar, while a weather station (produced by Davis Instruments) [50] equipped with a pyranometer was installed on the building roof to acquire outdoor air temperature, relative humidity, solar radiation, wind speed and direction.

Supply water temperature of the RF was collected through the probe used by the mixing valve, and thermal energy meters (produced by Maddalena) [51] equipped with two Pt100 probes were installed on the inlet and outlet of specific sections of the system (among them, the RF and the AHU) to acquire several data, like the instant and maximum flow rate, inlet temperature, outlet temperature, etc.

Furthermore, since December 2022 two heat flux meters were positioned over the floor in correspondence of a S27 (*HF_S27*) and a S17 (*HF_S17*) (Fig. 3). Technical data of the sensors mentioned above are

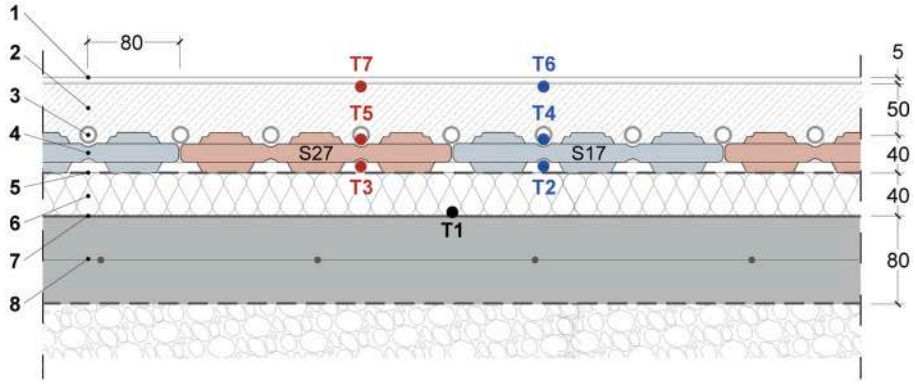

Fig. 4. RF configuration with PCMs and sensors position (layer thickness expressed in mm).

Fig. 5. Installation of the piping over PCMs.

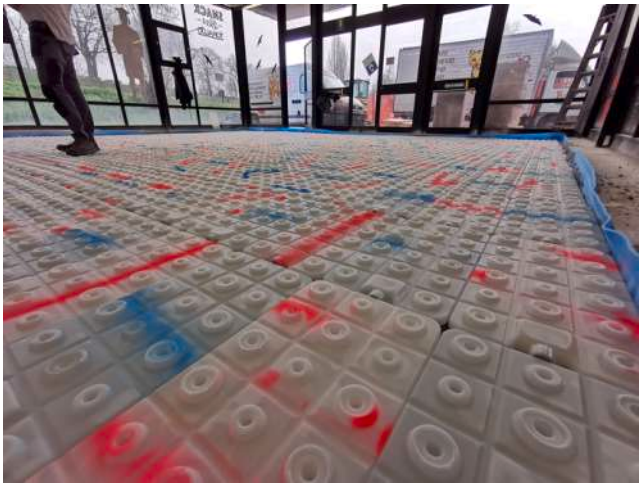

Fig. 6. ThinICE S27 (marked in red) alternated to ThinICE S17 (marked in blue). (For interpretation of the references to colour in this figure legend, the reader is referred to the web version of this article.)

reported in Table 4.

Thermocouples and heat flux meters were connected to a datalogger (produced by Delta Strumenti) [52] that acquired and saved data with a timestep of 30 s. Data saved by the datalogger, as well as the other data mentioned above, were acquired by means of different communication standards (Modbus line 1, Modbus line 2 and Modbus TCP), read every 30 s and used to write a database as a set of semicolon separated values, stored in the form of many.txt files, and saved at customised period of time.

Table 3
Floor structure materials and their thermophysical properties.

Material	Density kg/m^3	Specific heat kJ/(kg·K)	Thermal conductivity W/(m·K)
1. Vinyl flooring	1646	1.260	0.250
2. Dry-set mortar	2100	1.000	1.600
3. Piping	951	2.300	0–350
4. PCM S27* [46]	1530	2.200	0.540
PCM S17* [46]	1525	1.900	0.430
5. Vapor barrier	289	1.700	0.220
6. Insulation (XPS300)	31	1.450	0.033
7. Dump-proof membrane	923	–	–
8. Concrete slab	2400	0.900	1.500

*S27 latent heat = 185 kJ/kg.
S21 latent heat = 155 kJ/kg.

3. Results and discussion

The installation works of the IDEAS large-scale system started in October 2021 and were completed in June 2022 for the most part. However, being an experimental system, which included the installation of different components, most of them being innovative, the operation of the plant was characterised by long periods of testing for the implementation of the components and their tuning, as well as by highly frequent malfunctions or breakdowns of some devices. For these reasons, it has not been possible the conduct the monitoring for long and continuative periods, and comprehensive data about the thermal behaviour and energy consumption of the system for the entire heating or cooling periods are not available yet. Therefore, the most representative days for the cooling and the heating season were selected, and the main results are reported in section 3.1 and in section 3.2. The following parameters are reported in the charts illustrated in Fig. 7 to Fig. 15: indoor air temperature is identified as *T_int* [°C], outdoor air temperature is named *T_ext* [°C], supply water temperature of the RF is *T_RF* [°C], temperatures measured under and over a ThinICE and under floor finishing in correspondence of a S17 are *T2, T4, T6* [°C] and in correspondence of a S27 are *T3, T5, T7* [°C]. Solar radiation is identified as *Solar rad.* [W/m^2], heat fluxes measured in correspondence of a S27 and of a S17 are named *HF_S27* and *HF_S17* [W/m^2], respectively. Operation of the AHU is represented by the curve identified as *AHU on–off*, while thermal energy provided by the RF and the AHU are identified as *AHU energy* and *RF energy* [kWh], which were calculated using Eq. (1):

Table 4
Technical data of the monitoring devices.

	Sensing area m^2	**Sensor thickness m**	**Measurement range W/m^2**	**Sensitivity (nominal) $V/(W/m^2)$**	**Rated operating temperature range °C**	**Uncertainty of calibration**
Heat flow meters [47]	8×10^{-4}	5.4×10^{-3}	−2000… + 2000	60×10^{-6}	−30 … + 70	± 3 % (k = 2)
	Variant with thermal material	**Accuracy °C**	**Measurement Range °C**			
T-type thermocouples [48]	Cu-CuNi (T)	0.5	–200 to + 350			
	T accuracy °C	**RH accuracy %**	**Measurement Range °C and %**	**Long-term stability**	**Permissible air humidity**	
Digital T and RH sensor [49]	± 0.2 at + 25 °C	± 2.0 (20…80 % RH) at + 25 °C; otherwise ± 3.0	0… + 50 °C 0…100 %	± 1 % per year	< 95 % RH, non-precipitating air	
	T accuracy °C	**RH accuracy %**	**Solar radiation accuracy %**			
Weather station [50]	±0.3	± 2.0	± 5.0			
	Volumetric flow rate accuracy %	**ΔT (measured) accuracy %**	**ΔT (calculator) accuracy %**			
Thermal energy meters [51]	± (2 + 0.02* q_m/q_n) → or ± 5 % if greater	± (0.5 + 0.15/ΔT)	± (0.5 + 0.05/ΔT)			

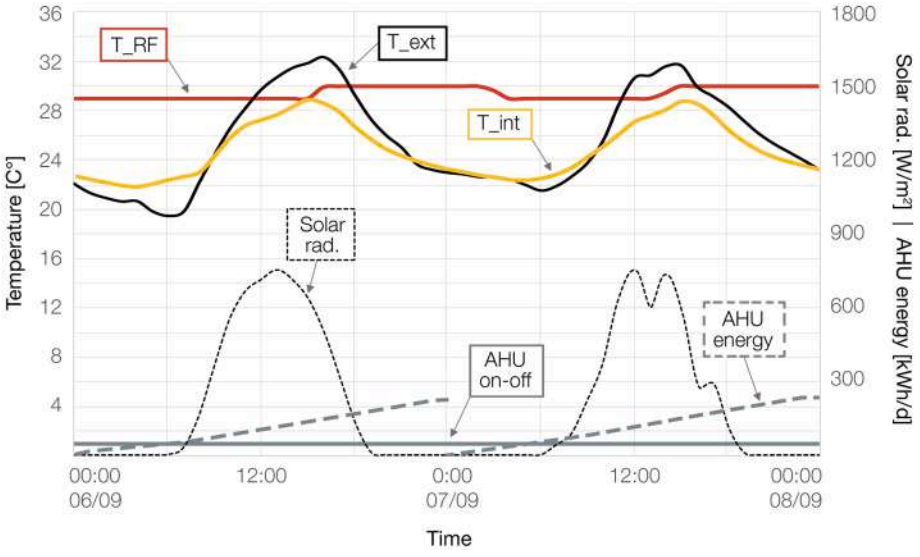

Fig. 7. Sole AHU operation, Sept. 6th–8th.

$$E_t = \left(\frac{\dot{m} \bullet c_p \bullet \Delta T}{3600}\right) \bullet t \quad (1)$$

where E_t is thermal energy [kWh], $\dot{m}$ is the volumetric flowrate [l/h], c_p is the specific heat [kJ/(kg·K)], ΔT is the temperature difference [K], and t is the operating time [h].

Finally, with the aim to verify if the latent heat storage capacity of PCMs was fully exploited, the comparison between values derived from the experimental data and those reported by the manufacturer was carried out in section 3.3.

3.1. Cooling period

The monitoring for the cooling period started from the end of June 2022. The AHU usually operated with a working fluid of 12 °C, whilst the RF optimised the supply water temperature to avoid the condensation over the floor, according to a control loop specifically developed. On average, the RF was able to ensure the cooling setpoint temperature of 26 °C in standard weather conditions, reaching an average power of around 40 W/m^2, with a maximum close to 60 W/m^2 to prevent condensation over the floor. The RF played a relevant smoothing role, on which the AHU only intervened to cover the thermal peaks, reaching an average power of around 6 kW in coupling with the RF.

A comparison between the two systems in terms of energy

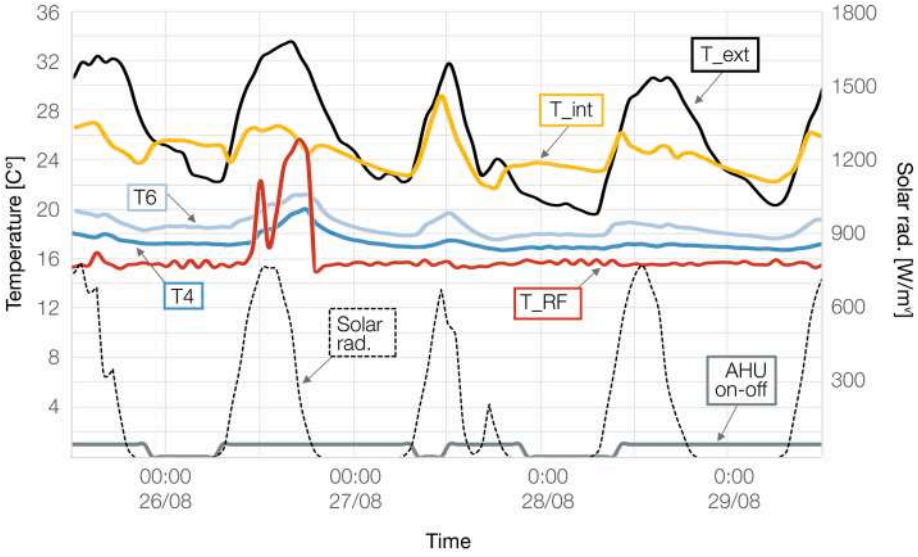

Fig. 8. AHU-RF operation, August 25th–30th.

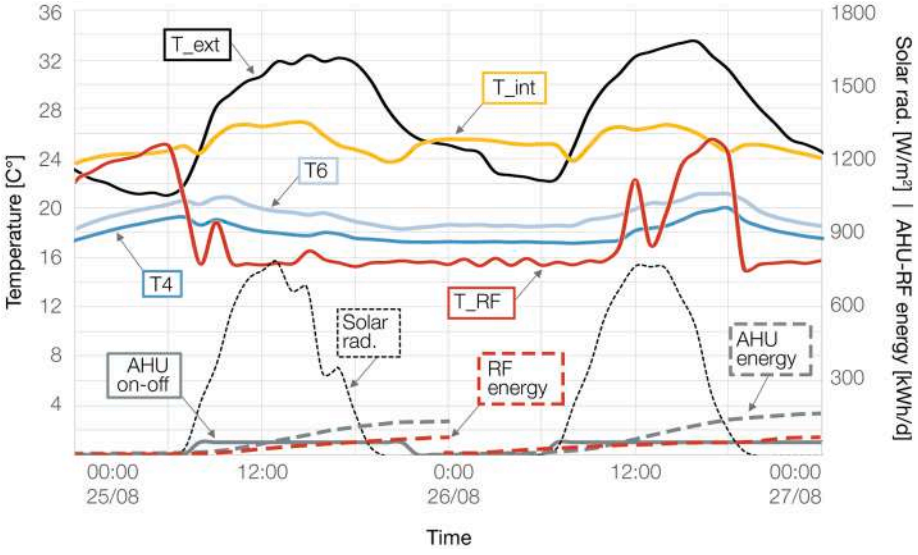

Fig. 9. AHU-RF operation, August 25th–27th.

performance and thermal comfort is reported in the following lines. Two periods characterised by comparable boundary weather conditions were selected. The operation of the sole AHU is reported in Fig. 7, which illustrates two days at the beginning of September, from 6th to 8th. Conversely, two days of end-August, from 25th to 27th, are illustrated in Fig. 9, when the AHU operation was integrated with the RF.

As regards AHU operation, despite an average outdoor air temperature of about 25.5 °C, the system was kept on throughout the two days considered. Nevertheless, the cooling setpoint temperature of 26 °C was barely ensured. Indoor air temperature ranged from 22 °C in the night up to 28 °C during the day (Fig. 7). Thermal energy supplied by the AHU was equal to 445 kWh. The same thermal performance was observed for the previous 40 h.

Differently, the last week of August was characterised by hard weather conditions, with outdoor air temperature reaching nearly 34 °C during the day, as illustrated in Fig. 8. A focus on two days, August 25th-27th, is reported in Fig. 9. On August 25th the RF and the AHU were turned on at about 8:00. Then, the AHU was switched off after the sunset (21:00), while the RF was kept operating. Keeping the RF on even after the turning off of the AHU allowed to maintain the indoor air temperature close to the setpoint of 26 °C during the night thanks to PCM solidification. Indeed, the temperature of outdoor air significantly decreased in the evening and indoor temperature decreased as well up to less than 24 °C. At the same time, PCM solidification began, and the phase change resulted in the increase of indoor air temperature, which was maintained between 25.1 and 25.6 °C throughout the night, despite temperature of outdoor air significantly continued to decrease and reached 22 °C. In this way, a lower energy effort was then required to manage indoor air temperature at sunrise and ensure the cooling setpoint temperature in the morning. The same relevant impact on the control of indoor air temperature can be noticed during the night of August 28th (Fig. 8), when outdoor temperature decreased and reached less than 20 °C. Indoor temperature decreased as well up to less than 22 °C. However, PCM solidification and the release of latent heat maintained indoor temperature between 23.5 and 23.7 °C. This behaviour clearly represents the possibility of an efficient and effective thermal storage carried out by the RF. On the contrary, this beneficial effect of PCM did not happen during the night of August 27th and 29th, when AHU was kept on and indoor air temperature continued to drop throughout the night reaching 22 °C (Fig. 8).

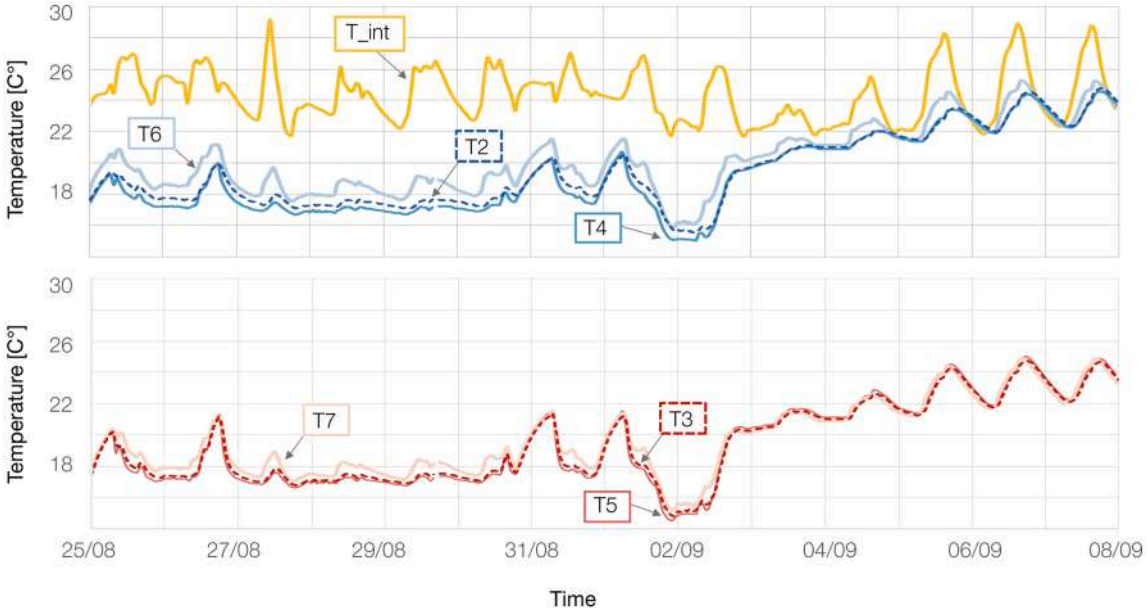

Fig. 10. Temperature at different layers of the RF structure.

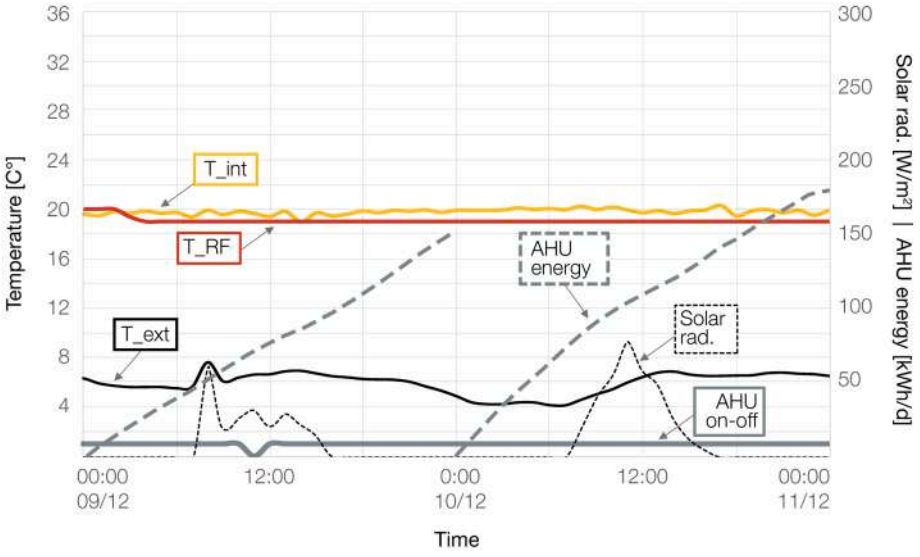

Fig. 11. Sole AHU operation, Dec. 9th–11th.

Focusing again on the two days of August 25th and 27th, the integration of the two systems allowed the AHU to be turned on for 31 h (Fig. 9), therefore 35 % less than the sole AHU operation. Thermal energy supplied by the AHU was equal to 287 kWh, while the one supplied by the RF was 136 kWh, achieving an energy saving of 5 %. Despite the small percentage, it should be noted that AHU and RF operated in hard weather conditions, with a mean outdoor temperature of 27.2 °C and solar energy gains of 11.4 kWh/m^2, thus considerably higher if compared to the period of sole AHU operation (Fig. 7), characterised by a mean outdoor temperature and solar energy of 25.5 °C and 10.1 kWh/m^2, respectively. In addition, the integration of the two systems allowed to achieve a significantly higher thermal comfort, with indoor air temperature ranging between 24 and 26 °C (Fig. 9).

However, PCM contribution did not consist only in the control of indoor air temperature during the night. Indeed, the turning off of the RF on August 26th at about 12:00 brought to the melting of PCM, which absorbed thermal load and allowed to achieve peak loads shaving and shifting. PCM reduced the cooling load to be covered by the AHU during peak price hours and stored thermal load to release it later in the night and control indoor temperature (Fig. 9).

The trend of the temperatures at the different layers in correspondence of S17 and S27 over a more extended time period, from August 25th to September 8th, is reported in Fig. 10, where the impact of S17 can be observed. Indeed, during S17 solidification, the temperature under S17 (T2) was higher than that under S27 (T3), thus highlighting the higher thermal resistance and related thermal inertia due to the phase change. The temperature difference demonstrated the thermal storage capacity of S17, whilst S27 is characterised only by the sensible thermal load. In addition, the temperature difference between the measuring points located under the floor finishing (T7), over (T5) and under S27 (T3) is very slight when temperatures are over 20 °C, whilst it is more relevant for the equivalent sensors positioned in correspondence of S17 (T6, T4 and T2). Furthermore, even if S17 was installed only on half of the floor surface, it was able to drive the temperature up to

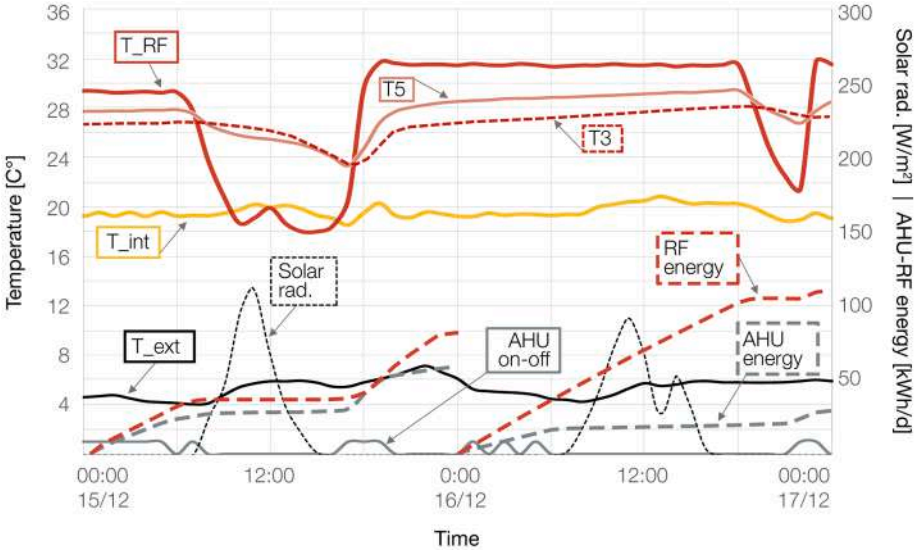

Fig. 12. AHU-RF operation, Dec. 15th–17th.

highlight a sub-cooling effect, when the piping forced the system to lower temperatures.

3.2. Heating period

The heating season was monitored from the end of November 2022 until February 1st, 2023. According to the climatic zone to which the city of Ferrara belongs, the heating period officially begins on October 15th. Nevertheless, the heating system did not operate until the end of November 2022, due to the unusually very high outdoor air temperatures.

On average, the indoor temperature setpoint was set at 20 °C, which was mainly ensured by the RF operating at a supply water temperature of 32 °C, reaching a daily thermal energy of around 104 kWh. This daily energy corresponded to an average thermal power of about 45 W/m^2, which sometimes was dramatically increased (up to higher values of 80 W/m^2) to test the limits of the RF and highlight the PCM thermal behaviour. The AHU was occasionally turned on by the algorithm (which includes the control rules for the exploitation of the different thermal sources) to cover very low outdoor air temperatures or to quickly recover the indoor setpoint temperature after the stop of the system for testing activities. More in detail, when the outdoor air temperature was less than 5 °C, the sole RF was not able to meet the building energy demand (>100 kWh/day), and the AHU was required to reach the indoor setpoint temperature. Differently, when outdoor air temperature ranged between 5 °C and 15 °C, the RF maintained the setpoint temperature alone. Finally, when the outdoor air temperature was higher than 15 °C, overheating conditions occurred due to the thermal inertia of the RF.

A comparison between the thermal performance of the two systems, the sole AHU and the AHU integrated with the RF, is carried out in the following lines. Again, two periods characterised by comparable boundary weather conditions were selected: from December 9th to 11th for the AHU operation (Fig. 11) and from 15th to 17th for the AHU-RF operation (Fig. 12). Both the periods presented similar average daily outdoor air temperature (5.9 °C and 5.3 °C respectively) and slight solar gains. Taking into consideration the AHU operation (Fig. 11), it was necessary to maintain the system continuously on for 48 h in order to ensure the setpoint temperature of 20 °C. The achieved mean indoor air temperature was 19.8 °C. Thermal energy supplied by the AHU was

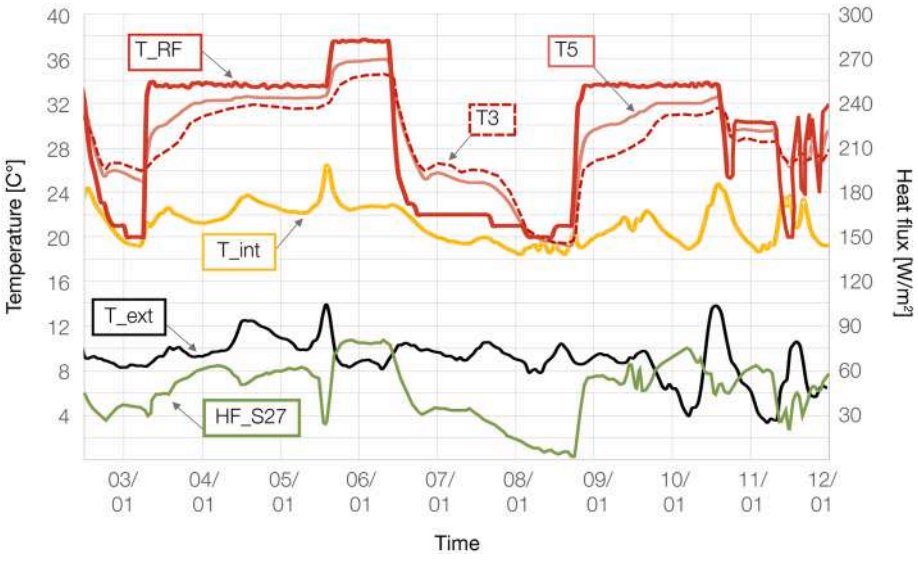

Fig. 13. Sole RF operation, January 2nd–12th.

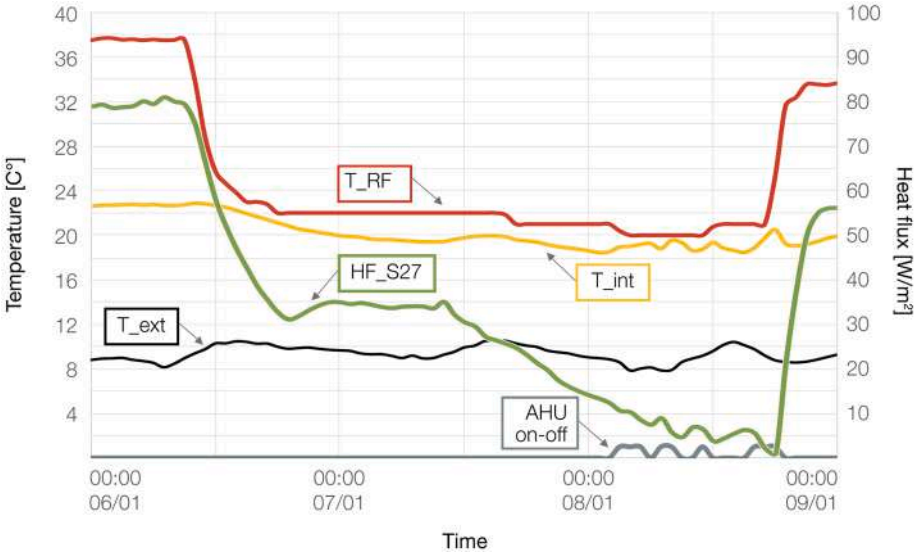

Fig. 14. RF turned off, PCM solidification.

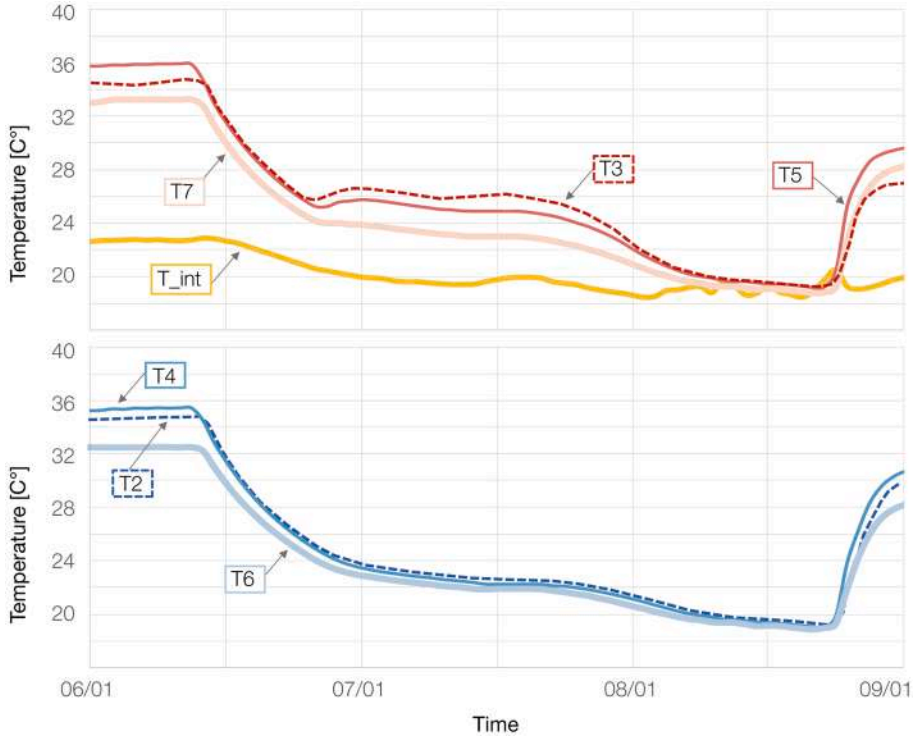

Fig. 15. Temperature at different layers of the RF structure, RF turned off.

equal to 331 kWh. Thermal energy was evaluated according to Eq. (1) reported in section 3.

Differently, the coupling between the two systems (Fig. 12) allowed to keep the AHU on only for 15 h, therefore 70 % less time than the first period analysed. The RF was maintained on for 34 h. It was turned off on December 15th at 6.00, along with the AHU, considered the solar gains contribution and the related increase of 2 °C in outdoor air temperature. The PCM solidification and release of latent heat allowed to maintain the setpoint temperature of 20 °C for 9 h after the switching off of the systems, which were turned on again at about 18:00. The RF was kept on for the following 24 h, whilst the AHU was on only for 6 h. In the coupled operation, thermal energy supplied by the AHU was equal to 86 kWh, while the one supplied by the RF was 200 kWh, resulting in a total thermal energy of 286 kWh. Thus, compared to the sole AHU operation, which presented a thermal energy of 331 kWh, the AHU-RF operation allowed to achieve an energy saving of 13 %. A similar value was reported in Ref. [19], where achievable heating energy saving ranging from 7.3 to 15.3 % were declared with 20–50 mm PCM positioned under piping, as reported in Table 1. However, in Ref. [19] a RF system not combined with an AHU was considered. Differently, lower energy savings (4 % on heating and 8 % on cooling) were evaluated in Ref. [39], where ThinICE filled with S27 and S21 were adopted for the heating and the cooling period, respectively. However, the system was installed in a 10 m^2 experimental mock-up building and PCM containers were positioned with three different distributions: a portion of the floor surface included only S27, another portion was characterised only by S21, in a

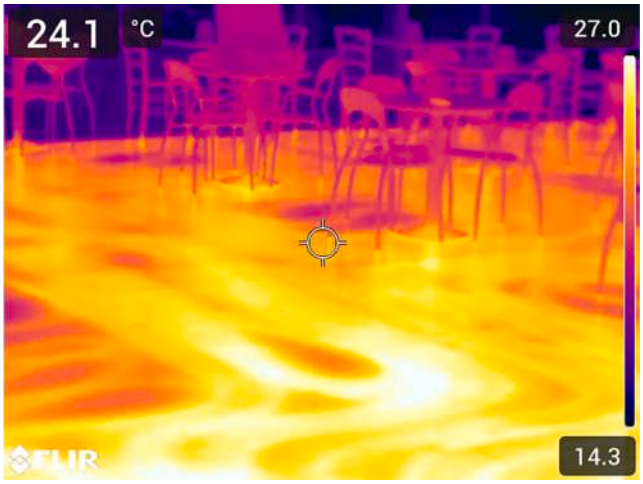

Fig. 16. RF on: piping emitting heat.

Fig. 17. RF off: effect of S27 against S17.

third portion S27 and S27 were positioned in a checkerboard pattern. Moreover, the mentioned energy savings may be achieved through the adoption of a control strategy based on weather forecast.

A 10 days-period representative of the sole RF operation, from January 2nd to 12th, is reported in Fig. 13, where three different conditions are illustrated. A standard performance of the system can be observed from January 3rd to 5th, when the adoption of a working fluid of about 32 °C resulted in a maximum heat flux of 63 W/m^2 and an average thermal energy of nearly 120 kWh/day. A high performance was achieved from January 5th to 6th, when the system operated at a supply water temperature of almost 36 °C, able to provide a maximum heat flux of 81 W/m^2 and an energy of 134 kWh/day. Finally, the PCM thermal storage performance occurred from January 6th to 8th, once the RF was turned off for a long time (56 h).

A focus on the single days when the radiant floor was turned off is illustrated in Fig. 14. The system was switched off on January 6th at 10:00. A steady heat flux of 35 W/m^2 was ensured for almost 13 h, and setpoint temperature of 20 °C was maintained until January 7th at 16:00, thus for nearly 30 h after the switching off of the system. The subcooling effect was evident not only considering the temperatures but also the heat flux, which initially decreased up to 31 W/m^2. The impact of PCM solidification and heat release can be observed also when analysing the temperatures at different layers of the RF structure, as reported in Fig. 15. Indeed, temperature under (T3) and over (T5) S27 are higher than the those under (T2) and over (T4) S17. Furthermore, the temperature under floor finishing (T7) in correspondence of S27 is maintained between 22 and 24 °C, with a room temperature equal to about 20 °C. These results are similar to those achieved in Ref. [36], where floor temperature was ensured in the range 18–24 °C with a room temperature of 19 °C, as reported in Table 1. However, in the system analysed in Ref. [36] the cold storage layer was positioned above the heat storage one, and both encased piping network.

Thermography reported in Fig. 16 and in Fig. 17 highlights the effect of the S27 against the S17 when the RF is turned off after its operation. Indeed, when the system is operating, only the heat emitted by the piping network is evident (Fig. 16). Then, when the RF is switched off and PCM solidification begins, the S27 release a large quantity of thermal energy by using latent heat during the phase change, whilst S17 just emits sensible heat. Therefore, the chequerboard layout can be clearly observed (Fig. 17).

3.3. Exploitation of the PCMs latent heat capacity

In order to evaluate if the PCMs capacity of latent heat storage was fully exploited, the comparison between the values of latent heat derived from the monitoring data and those provided by the manufacturer was conducted.

Differential scanning calorimetry (DSC) curves of the two PCMs, provided by the manufacturer PCM Products Ltd [45], are illustrated in Fig. 18 and Fig. 19, where a value of latent heat equal to 185.51 kJ/kg and 156.64 kJ/kg is reported for S27 and S17, respectively.

Two representative days, one during the heating and one during the cooling period, that were characterised by the sole operation of the RF system and the phase transition of PCM due to the turning off of the system were identified in 20th March 2023 and in 30th June 2023. Latent heat ΔH_{SL} [kJ/kg] was evaluated using Eq. (2):

$$\Delta H_{SL} = \frac{\int_{t_1}^{t_2} \dot{q}_{tot} dt - \sum_{i=1}^{n} (\mathrm{m}_i \bullet c_{p_i} \bullet \Delta T_i)}{m_{PCM}} \quad (2)$$

where t_1 and t_2 are the beginning and the end of the phase change process, $\dot{q}_{tot}$ [kW/m^2] is the heat flux through the floor, n is the number of floor layers, m_i is the material mass per unit surface area of the layer i [kg/m^2] obtained as the product between density ρ [kg/m^3] and the equivalent thickness of the material Δx [m], c_{p_i} is the specific heat [kJ/(kg·K)], and ΔT_i is the temperature difference [K], m_{PCM} is the PCM mass per unit surface area [kg/m^2].

As for m_{PCM} [kg/m^2], the following parameters provided by the manufacturer PCM Products Ltd [44] were considered (Table 5):

Taking into consideration the data reported above, the following values of ΔH_{SL} were achieved and compared to the values reported by the manufacturer (Table 6):

The percentage of discrepancy, although quite small, between the values of ΔH_{SL} derived from experimental data and those declared by the manufacturer can be due to the fact that the space monitored was often occupied by a high number of people which impacted on the monitoring. Furthermore, despite the insulation layer positioned below PCMs, thermal dispersions occurred. Therefore, the slight difference between the measured and the provided values of ΔH_{SL} demonstrated that the latent heat storge capacity of PCMs was almost fully exploited. Moreover, the consistency of the values obtained highlights the reliability of the results here presented and demonstrates the significance of the study conducted.

4. Conclusions

The thermal performance of a radiant floor (RF) heating and cooling system enhanced with two PCM types, one for the winter and one for the summer period, has been experimentally investigated at full-scale by the University of Ferrara within the H2020 European project IDEAS. The PCM-RF system was installed in a 100 m^2 academic snack-bar selected as

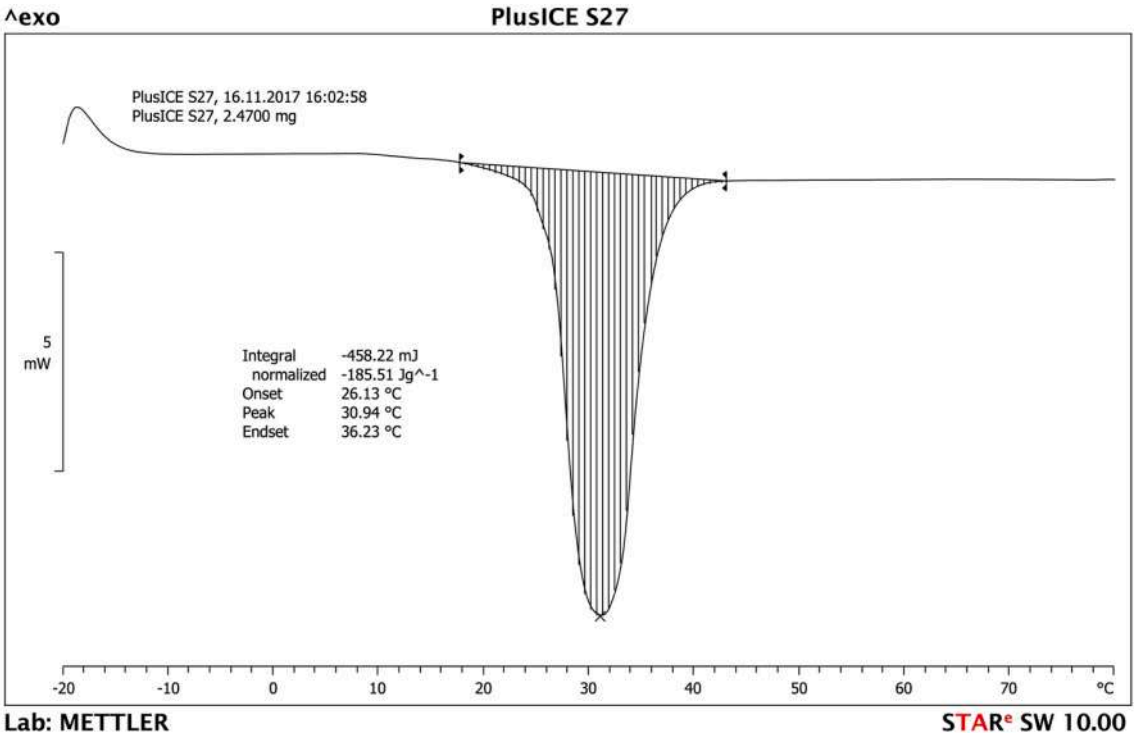

Fig. 18. DSC curve of S27 (source: PCM Products Ltd [45]).

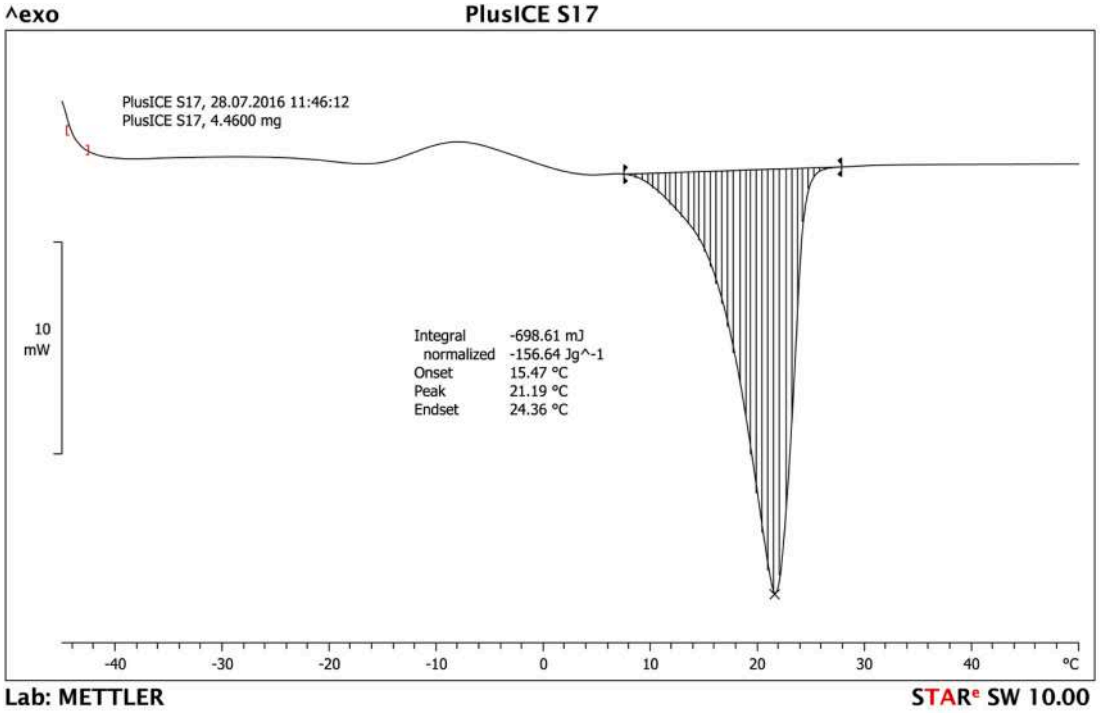

Fig. 19. DSC curve of S17 (source: PCM Products Ltd [45]).

Table 5
Technical data about ThinICE.

PCM	Quantity of ThinICE per m^2	PCM mass per ThinICE kg	PCM mass per m^2 kg/m^2
S27	4	2.49 [44]	9.96
S17	4	2.48 [44]	9.92

building demonstrator, monitored since end-June 2022. The system was composed of macroencapsulated hydrated salts with a melting temperature of 27 °C for winter and of 17 °C for summer, which were installed according to a checkerboard pattern. The space was equipped with an existing air handling unit (AHU) to ensure ventilation rates and manage latent loads.

The following conclusions and observations have been derived from

Table 6
Comparison between ΔH_{SL} derived from experimental data and values declared by the manufacturer.

PCM	Experimental ΔH_{SL} kJ/kg	Declared ΔH_{SL} kJ/kg	Discrepancy
S27	166.08	185.51	10 %
S17	142.49	156.64	9 %

the present study and should be considered to foster and support the design of future applications:

- Results obtained from the analysis of the monitoring data highlighted the effective thermal storage capacity of PCM integrated in the RF system, both in the heating and in the cooling period.
- In summer, the turning off of the RF at midday brought to the melting of PCM, which absorbed thermal loads, thus achieving peak loads shaving and shifting. Indeed, in this way PCM reduced the cooling load to be covered by the AHU during peak price hours, and was able to release thermal loads later in the night. Indeed, the switching off of the AHU after the sunset, with the RF still on, brought to PCM solidification, release of thermal loads and maintenance of the indoor air temperature close to the setpoint of 26 °C throughout the night. In this way, a lower energy effort was required to the AHU at sunrise in order to ensure the cooling setpoint temperature.
- In winter, operation of the AHU integrated with the RF allowed to achieve 13 % energy savings if compared to the sole AHU operation. Indeed, PCM thermal storage allowed to keep AHU on for 70 % less time and to maintain the setpoint temperature of 20 °C for 9 h after the switching off of both the systems. Furthermore, taking into consideration the sole operation of the RF, the system was able to maintain the setpoint temperature for almost 30 h after the switching off.

The experimental results of a real-scale installation are reported for the first time in the present manuscript. In addition, the coupling technology employed in the snack-bar represents a real example of renovation, which integrates the possibility of high thermal storage of macro-encapsulated PCMs within a particularly limited thickness of the floor due to existing structural constraints. Finally, in order to aid a proper interpretation of the achieved results, it should be considered the poor building envelope of the snack-bar where the application was conducted, which confirms the significant energy saving potential. Therefore, the work could be exploited to lay the basis for the design of far more optimised systems and to develop a design framework for a more extensive application of PCM enhanced radiant floor systems, especially considered the energy savings achievable through the adoption of these low-temperature heating and high-temperature cooling systems, as well as the potential exploitation of renewable energy sources.

Being an experimental system, the operation of the plant was often characterised by long periods of testing for the implementation of the components, as well as by highly frequent malfunctions or breakdowns of some devices. For these reasons, it has not been possible the conduct the monitoring for long and continuative time periods and the analysis could be conducted only on the base of the most representative days for the cooling and the heating season. Therefore, one of the future developments of the study will be the analysis of continuous and regular monitoring campaign (currently ongoing), in order to be able to evaluate comprehensive data about the thermal behaviour and energy consumption of the system for whole heating and cooling periods.

CRediT authorship contribution statement

Silvia Cesari: Writing – review & editing, Writing – original draft, Visualization, Investigation. **Eleonora Baccega:** Validation, Methodology, Data curation. **Giuseppe Emmi:** Supervision. **Michele Bottarelli:** Supervision, Funding acquisition, Data curation, Conceptualization.

Declaration of competing interest

The authors declare that they have no known competing financial interests or personal relationships that could have appeared to influence the work reported in this paper.

Data availability

The data that has been used is confidential.

Acknowledgements

This work was supported financially within the IDEAS project – Novel building Integration Designs for increased Efficiencies in Advanced Climatically Tunable Renewable Energy Systems. This project is funded by the European Union's Horizon 2020 research and innovation programme under grant agreement No. 815271.

References

[1] European Council. Energy prices and security of supply. https://www.consilium.europa.eu/en/policies/energy-prices-and-security-of-supply/, 2023 [Accessed 23 April 2023].
[2] European Commission. European Green Deal: EU agrees stronger legislation to accelerate the rollout of renewable energy. https://ec.europa.eu/commission/presscorner/detail/en/IP_23_2061, 2023 [Accessed 23 April 2023].
[3] P. Ovchinnikov, A. Borodiņecs, K. Strelets, Utilization potential of low temperature hydronic space heating systems: a comparative review, Build. Environ. 112 (2017) 88–89, https://doi.org/10.1016/j.buildenv.2016.11.029.
[4] J. Cho, B. Park, T. Lim, Experimental and numerical study on the application of low-temperature radiant floor heating system with capillary tube: thermal performance analysis, Appl. Therm. Eng. 163 (2019) 114360, https://doi.org/10.1016/j.applthermaleng.2019.114360.
[5] G.L. Szabó, F. Kalmár, Investigation of energy and exergy performances of radiant cooling systems in buildings - a design approach, Energy 185 (2019) 449–462, https://doi.org/10.1016/j.energy.2019.07.067.
[6] M. Bojić, D. Cvetković, V. Marjanović, M. Blagojević, Z. Djordjević, Performances of low temperature radiant heating systems, Energy Build. 61 (2013) 233–238, https://doi.org/10.1016/j.enbuild.2013.02.033.
[7] Y. Khan, V.R. Khare, J. Mathur, M. Bhandari, Performance evaluation of radiant cooling system integrated with air system under different operational strategies, Energy Build. 97 (2015) 118–128, https://doi.org/10.1016/j.enbuild.2015.03.030.
[8] A. Behzadi, S. Holmberg, C. Duwig, F. Haghighat, R. Ooka, S. Sadrizadeh, Smart design and control of thermal energy storage in low-temperature heating and high-temperature cooling systems: a comprehensive review, Renew. Sustain. Energy Rev. 166 (2022) 112625, https://doi.org/10.1016/j.rser.2022.112625.
[9] A. Charraou, S. Oubenmoh, A. Mourid, R. Saadani, M. Rahmoune, M. El Alami, Experimental study and numerical simulation of a floor heating system in a three-dimensional model: parametric study and improvement, Appl. Therm. Eng. 233 (2023) 121151, https://doi.org/10.1016/j.applthermaleng.2023.121151.
[10] S. Mousavi, B. Rismanchi, S. Brey, L. Aye, PCM embedded radiant chilled ceiling: a state-of-the-art review, Renew. Sustain. Energy Rev. 151 (2021) 111601, https://doi.org/10.1016/j.rser.2021.111601.
[11] E. Elnagar, A. Zeoli, R. Rahif, S. Attia, V. Lemort, A qualitative assessment of integrated active cooling systems: a review with a focus on system flexibility and climate resilience, Renew. Sustain. Energy Rev. 175 (2023) 113179, https://doi.org/10.1016/j.rser.2023.113179.
[12] A. Sharma, V.V. Tyagi, C.R. Chen, D. Buddhi, Review on thermal energy storage with phase change materials and applications, Renew. Sustain. Energy Rev. 13 (2009) 318–345, https://doi.org/10.1016/j.rser.2007.10.005.
[13] S.E. Kalnæs, B.P. Jelle, Phase change materials and products for building applications: a state-of-the-art review and future research opportunities, Energy Build. 94 (2015) 150–176, https://doi.org/10.1016/j.enbuild.2015.02.023.
[14] R. Ansuini, R. Larghetti, A. Giretti, M. Lemma, Radiant floors integrated with PCM for indoor temperature control, Energy Build. 43 (2011) 3019–3026, https://doi.org/10.1016/j.enbuild.2011.07.018.
[15] H. Zhang, J. Baeyens, G. Cáceres, J. Degrève, Y. Lv, Thermal energy storage: recent developments and practical aspects, Prog. Energy Combust. Sci. 53 (2016) 1–40, https://doi.org/10.1016/j.pecs.2015.10.003.
[16] K. Faraj, J. Faraj, F. Hachem, H. Bazzi, M. Khaled, C. Castelain, Analysis of underfloor electrical heating system integrated with coconut oil-PCM plates, Appl. Therm. Eng. 158 (2019) 113778, https://doi.org/10.1016/j.applthermaleng.2019.113778.
[17] M.T. Plytaria, C. Tzivanidis, E. Bellos, K.A. Antonopoulos, Parametric analysis and optimization of an underfloor solar assisted heating system with phase change

materials, Therm. Sci. Eng. Prog. 10 (2019) 59–72, https://doi.org/10.1016/j.tsep.2019.01.010.
[18] S. Baek, S. Kim, Determination of optimum hot-water temperatures for PCM radiant floor-heating systems based on the wet construction method, Sustain. 10 (2018) 4004, https://doi.org/10.3390/su10114004.
[19] S. Baek, S. Kim, Analysis of thermal performance and energy saving potential by PCM radiant floor heating system based on wet construction method and hot water, Energies 12 (2019) 828, https://doi.org/10.3390/en12050828.
[20] B. González, M.M. Prieto, Radiant heating floors with PCM bands for thermal energy storage: a numerical analysis, Int. J. Therm. Sci. 162 (2021) 106803, https://doi.org/10.1016/j.ijthermalsci.2020.106803.
[21] O. Babaharra, K. Choukairy, S. Hamdaoui, K. Khallaki, S.H. Mounir, Thermal behaviour evaluation of a radiant floor heating system incorporates a microencapsulated phase change material, Constr. Build. Mater. 330 (2022) 127293, https://doi.org/10.1016/j.conbuildmat.2022.127293.
[22] M. Zhao, T. Zhu, C. Wang, H. Chen, Y. Zhang, Numerical simulation on the thermal performance of hydraulic floor heating system with phase change materials, Appl. Therm. Eng. 93 (2016) 900–907, https://doi.org/10.1016/j.applthermaleng.2015.10.020.
[23] J. Mazo, M. Delgado, J.M. Marin, B. Zalba, Modeling a radiant floor system with phase change material (PCM) integrated into a building simulation tool: analysis of a case study of a floor heating system coupled to a heat pump, Energy Build. 47 (2012) 458–466, https://doi.org/10.1016/j.enbuild.2011.12.022.
[24] J. Park, T. Kim, Analysis of the thermal storage performance of a radiant floor heating system with a PCM, Mol. 24 (2019) 1352, https://doi.org/10.3390/molecules24071352.
[25] En 1264–3:2021., Water based surface embedded heating and cooling systems - part 3, Dimensioning (2021).
[26] G. Zhou, J. He, Thermal performance of a radiant floor heating system with different heat storage materials and heating pipes, Appl. Energy 138 (2015) 648–660, https://doi.org/10.1016/j.apenergy.2014.10.058.
[27] M. Yamaguchi, S. Sayama, H. Yoneda, M. K-y Iwamoto, S. Harada, K.F. Watanabe, Heat storage-type floor heating system with heat pump driven by nighttime electric power, Heat Transf. Jpn. Res. 26 (1997) 122–130, 10.1002/(SICI)1520-6556(1997)26:2<122::AID-HTJ6>3.0.CO;2-Y.
[28] S. Baek, J.C. Park, Proposal of a PCM underfloor heating system using a web construction method, Int. J. Polym. Sci. 2017 (2017) 2693526, https://doi.org/10.1155/2017/2693526.
[29] M. Farid, W.J. Kong, Underfloor heating with latent heat storage, Proc. Inst. Mech. Eng. a: J. Power Energy 215 (2001) 601–609, https://doi.org/10.1243/0957650011538839.
[30] B. Larwa, S. Cesari, M. Bottarelli, Study on thermal performance of a PCM enhanced hydronic radiant floor heating system, Energy 225 (2021) 120245, https://doi.org/10.1016/j.energy.2021.120245.
[31] E. Baccega, M. Bottarelli, S. Cesari, Addition of granular phase change materials (PCMs) and graphene to a cement-based mortar to improve its thermal performances, Appl. Therm. Eng. 229 (2023) 120582, https://doi.org/10.1016/j.applthermaleng.2023.120582.
[32] S. Lu, B. Xu, X. Tang, Experimental study on double pipe PCM floor heating system under different operation strategies, Renew. Energy 145 (2020) 1280–1291, https://doi.org/10.1016/j.renene.2019.06.086.
[33] S. Lu, J. Gao, H. Tong, S. Yin, X. Tang, X. Jiang, Model establishment and operation optimization of the casing PCM radiant floor heating system, Energy 193 (2020) 116814, https://doi.org/10.1016/j.energy.2019.116814.
[34] Y. Xu, B.B. Sun, L.J. Liu, X.Y. Liu, The numerical simulation of radiant floor cooling and heating system with double phase change energy storage and the thermal performance, J. Energy Storage 40 (2021) 102635, https://doi.org/10.1016/j.est.2021.102635.
[35] X. Jin, X. Zhang, Thermal analysis of a double layer phase change material floor, Appl. Therm. Eng. 31 (2011) 1576–1581, https://doi.org/10.1016/j.applthermaleng.2011.01.023.
[36] F. Ren, J. Du, Y. Cai, Z. Xu, D. Zhang, Y. Liu, Numerical simulation study on thermal performance of sub-tropical double-layer energy storage floor combined with ceiling energy storage radiant air conditioning, Case Stud. Therm. Eng. 28 (2021) 101696, https://doi.org/10.1016/j.csite.2021.101696.
[37] W. Sun, Y. Zhang, Z. Ling, X. Fang, Z. Zhang, Experimental investigation on the thermal performance of double-layer PCM radiant floor system containing two types of inorganic composite PCMs, Energy Build. 211 (2020) 109806, https://doi.org/10.1016/j.enbuild.2020.109806.
[38] Y. Xia, X.S. Zhang, Experimental research on a double-layer radiant floor system with phase change material under heating mode, Appl. Therm. Eng. 96 (2016) 600–606, https://doi.org/10.1016/j.applthermaleng.2015.11.133.
[39] S. Cesari, G. Emmi, M. Bottarelli, A weather forecast-based control for the improvement of PCM enhanced radiant floors, Appl. Therm. Eng. 206 (2022) 118119, https://doi.org/10.1016/j.applthermaleng.2022.118119.
[40] IDEAS - Novel building Integration Designs for increased Efficiencies in Advanced Climatically Tunable Renewable Energy Systems. https://www.horizon2020ideas.eu [Accessed 23rd April 2023].
[41] European publication server, EP2418439. https://data.epo.org/publication-server/document?PN=EP2418439%20EP%202418439&iDocId=4172968&iPosition=0&iFormat=2 [Accessed 23rd November 2023].
[42] M. Bottarelli, M. Bortoloni, Y. Su, On the sizing of a novel flat-panel ground heat exchanger in coupling with a dual-source heat pump, Renew. Energy 142 (2019) 552–560, https://doi.org/10.1016/j.renene.2019.04.088.
[43] M. Bottarelli, E. Baccega, S. Cesari, G. Emmi, Role of phase change materials in backfilling of flat-panels ground heat exchanger, Renew. Energy 189 (2022) 1324–1336, https://doi.org/10.1016/j.renene.2022.03.061.
[44] ThinICE Phase Change Material. https://www.pcmproducts.net/files/ThinICE.pdf [Accessed 23rd April 2023].
[45] PCM Products Ltd. https://www.pcmproducts.net [Accessed 23rd April 2023].
[46] PCM Products Ltd. PlusICE Hydrated Salt (S) Range. https://www.pcmproducts.net/files/PlusICE%20Range%202021-1.pdf [Accessed 23rd April 2023].
[47] Hukseflux Thermal Sensors. HFP01 heat flux sensor. https://www.hukseflux.com/products/heat-flux-sensors/heat-flux-meters/hfp01-heat-flux-sensor [Accessed 23rd April 2023].
[48] Delta Strumenti. Thermocouple wire (in Italian). https://www.deltastrumenti.it/images/pdf/termocoppie/in_cavetto/Termocoppia_cavetto.pdf [Accessed 23rd April 2023].
[49] S+S Regeltechnik. Room humidity and temperature sensor HYGRASGARD RFTF – Modbus. https://www.spluss.de/en/room-humidity-and-temperature-sensor-hygrasgard-rftf-modbus-modbus-d201-42b6-0000-000-p4159/ [Accessed 23rd April 2023].
[50] Davis Instruments. Weather station Vantage Pro2. https://www.davisinstruments.com/vantage-pro2/ [Accessed 23rd April 2023].
[51] Maddalena. Ultrasonic compact thermal energy meter Microclima U. https://www.maddalena.it/en/product/microclima-u/ [Accessed 23rd April 2023].
[52] Delta Strumenti. DT80 Series 4 Data Logger. https://www.deltastrumenti.it/images/pdf/datataker/dataTaker_DT80.pdf [Accessed 23rd April 2023].